Spectral imaging of proton aurora and twilight at Tromsø, Norway

M. Galand,[1] J. Baumgardner,[1] D. Pallamraju,[1] S. Chakrabarti,[1] U. P. Løvhaug,[2] D. Lummerzheim,[3] B. S. Lanchester,[4] and M. H. Rees[4]

[1]   An imaging Echelle spectrograph designed for high-resolution studies of selected spectral features located in the visible spectrum was deployed from November 2001 until April 2003 in Tromsø, Norway. For moderately disturbed magnetic conditions, Tromsø is located on the equatorial edge of the evening auroral oval for several hours. Energetic protons are frequently the dominant particle energy source in this region. For this experiment, four spectral windows were selected, each around different emission features: H_α (656.3 nm), H_β (486.1 nm), N_2^+1NG 427.8 nm, and OI 777.4 nm. The $8°$ long slit of the spectrograph was centered on the magnetic zenith. This instrument provided simultaneous, high-resolution ($\sim$0.1 nm) spectra of H_α and H_β emissions, which offers a unique opportunity to investigate the H_α to H_β Balmer decrement in proton aurora. Information on the cloud cover and on the overall auroral activity was provided by a large field of view ($70°$) conventional imaging spectrograph that spans the $350-800$ nm spectral range. In this paper we describe both instruments and demonstrate their capabilities for the study of the H Balmer emissions in twilight and during auroral activity. Our high-resolution spectra taken in twilight could be used to observe the variability of the geocoronal component over time and to compare the derived variability with midlatitude sites. We conclude that the 0.1 nm spectral resolution is sufficient to identify and take into account contaminating OH and N_2 1PG features in H_α emission profiles. Comparison of H_β Doppler profiles observed at different locations (Tromsø, Poker Flat, Svalbard) in proton aurora is presented. *Lummerzheim and Galand* [2001] find that the shape of the violet wing of the Balmer profile is a more suitable indicator of the mean energy of the incident protons than the Doppler shift of the peak. Numerous uncertainties in measured and modeled H_α and H_β line profiles preclude using the Balmer decrement as an indicator of the precipitating proton flux.   *INDEX TERMS:* 2407 Ionosphere: Auroral ionosphere (2704); 2455 Ionosphere: Particle precipitation; 2494 Ionosphere: Instruments and techniques; 2431 Ionosphere: Ionosphere/magnetosphere interactions (2736); *KEYWORDS:* proton aurora, auroral spectroscopy, geocoronal emission, calibration technique, H Balmer lines, Balmer decrement

1.   Introduction

[2]   The European Incoherent Scatter (EISCAT) radar probing the high-latitude ionosphere is located near Tromsø, Norway, at 66.4°N magnetic latitude. For moderately magnetically disturbed conditions ($Kp = 2-3$), it is situated for several hours at the equatorial edge of the evening auroral oval, where energetic protons are usually the dominant

particle energy source [e.g., *Hardy et al.*, 1989]. *Senior* [1991] compared the height-integrated conductivities derived from EISCAT data with a statistical model of conductances obtained from precipitating electron characteristics measured by the polar-orbiting Defense Meteorological Satellite Program (DMSP) [*Hardy et al.*, 1987]. *Senior* [1991] found that the EISCAT-derived conductances agree well with the DMSP model in the morning sector but are systematically larger than the model in the evening sector. She suggested that this difference is due to E region electron production by energetic ion precipitation, which occurs preferentially in the evening sector. Using simultaneous observations from a space-based particle detector and from the EISCAT radar, *Lilensten and Galand* [1998] have shown that protons are sometimes the major source of ionization above Tromsø. Recently, *Galand et al.* [2001]

[1]Center for Space Physics, Boston University, Boston, Massachusetts, USA.
[2]Department of Physics, University of Tromsø, Tromsø, Norway.
[3]Geophysical Institute, University of Alaska, Fairbanks, Alaska, USA.
[4]Department of Physics, University of Southampton, Southampton, UK.

used statistical patterns of both electron and ion characteristics to drive a three-dimensional, time-dependent, coupled model of the thermosphere and ionosphere to assess the influence of proton precipitation on Earth's auroral upper atmosphere. They found that owing to the offset of the proton auroral oval toward dusk, during moderate magnetic activity ($Kp = 2-3$), precipitating protons can carry most of the energy in the equatorial edge of the evening sector of the auroral oval. This study has corroborated the contribution of protons to the conductances at the location of the EISCAT radar.

[3] When no simultaneous in situ particle data from satellite overpasses are available, the incoherent scatter radar can be used to detect the presence of particle precipitation, but it cannot identify the type of the incoming particles. Doppler-shifted H emissions are a unique signature of proton precipitation [e.g., *Eather*, 1967]. Their ground-based discovery was the first evidence of proton precipitation in the auroral regions [*Vegard*, 1948; *Meinel*, 1951]. The H emission profile viewed along the magnetic zenith from the ground (space) is Doppler shifted with its peak blue (red) shifted, resulting from excited energetic H atoms inside the proton beam. From space, Lyman α is the brightest H emission in proton aurora and has been observed by numerous satellites [e.g., *Paresce et al.*, 1983; *Ishimoto et al.*, 1989; *Strickland et al.*, 2001; *Galand et al.*, 2002]. The first global imaging of the entire proton auroral oval was offered by the Spectrographic Imager (SI) 12 instrument on board Imager for Magnetopause-to-Aurora Global Exploration (IMAGE) [e.g., *Frey et al.*, 2001; *Mende et al.*, 2001]. However, either owing to low ($\sim$1 nm) spectral resolution [*Galand et al.*, 2002] or to the lack of spectral profile due to spectral filtering [*Frey et al.*, 2001], the energy spectrum (including the mean energy) of the incoming protons needs to be assumed. This limits the analysis of observations taken from space in terms of quantitative inference of the incident proton energy flux.

[4] From the ground, H Lyman lines cannot be detected due to atmospheric absorption, so H Balmer lines are used instead. Measurements of their total brightness are used to study spatial distributions and temporal variations of proton aurora and to probe magnetospheric processes, especially during substorms [e.g., *Vallance-Jones et al.*, 1982; *Samson et al.*, 1992; *Deehr and Lummerzheim*, 2001; *Takahashi and Fukunishi*, 2001]. As for spectrometric observations, even though the H_α line at 656.3 nm is the brightest Balmer line, its spectral proximity to the bright N_2 first positive and the OH airglow bands makes it difficult to obtain unambiguous line profiles. Therefore the spectral profile of the Balmer line H_β at 486.1 nm is the most commonly used in the study of proton aurora [*Zwick and Shepherd*, 1963; *Eather*, 1967; *Deehr et al.*, 1998; *Lorentzen et al.*, 1998; *Lummerzheim and Galand*, 2001; *Lanchester et al.*, 2003]. The H profiles observed several decades ago in the magnetic zenith had a low spectral resolution ($\sim$1 nm) [e.g., *Eather*, 1967]. The Doppler-shifted red wing in these early observations can be explained by the instrumental function of the spectrographs used [*Galand et al.*, 1998]. Recent comprehensive spectral analysis of the proton aurora, however, has revealed a physical origin of the red wing. *Lummerzheim and Galand* [2001] and *Lanchester et al.* [2003] showed that the Doppler-shifted red wing observed at higher spectral resolution (<0.5 nm) is produced by upflowing energetic

H atoms. Comparing the observations to calculations from a comprehensive proton transport model, these authors demonstrated that the upward flux is produced by collisional angular scattering within the proton beam. Originally, the magnitude of the Doppler shift of the peak of the profile was thought to be an indicator of the mean energy of the incoming protons [e.g., *Eather*, 1967]. Using their high-spectral-resolution observations, *Lummerzheim and Galand* [2001] found that the shape of the violet wing (shortward of the blue-shifted peak) is a more suitable indicator of the hardness of the precipitation. This conclusion was confirmed by *Lanchester et al.* [2003], who compared ground-based H_β Doppler profiles with in situ particle data from almost coincident passes from the FAST and DMSP spacecrafts.

[5] The Balmer decrement, defined as the ratio of the total brightness of the H_α to H_β lines in proton aurora, has been the focus of both experimental and theoretical studies for the last 40 years [e.g., *Eather*, 1967; *Rees*, 1982; *Van Zyl et al.*, 1984; *Srivastava and Singh*, 1987; *Sigernes et al.*, 1994a, 1994b; *Sigernes et al.*, 1996, and references therein]. This ratio could, in principle, yield information on the spectral characteristics of the incoming protons [*Sigernes et al.*, 1996]. *Sigernes et al.* [1994a, p. 507] pointed out that the "influence of airglow OH(6, 1) and auroral N_2 1PG in the region of H_α makes high resolution spectra necessary to obtain the true observed ratio between H_α and H_β." *Sigernes et al.* [1996] derived a value for the Balmer decrement by comparing the H_α brightness measured by a high-spectral-resolution (0.2 nm) spectrometer with the H_β brightness measured by a Meridian Scanning Photometer. They observed large variation over time of the Balmer decrement and concluded that [*Sigernes et al.*, 1996, p. 1289] "in order to obtain true ratios between H_α and H_β it is necessary to measure the total Doppler shifted and broadened profiles with high resolution and sensitive spectrometers." Since their paper, there has been no published investigation of the Balmer decrement to our knowledge.

[6] We deployed a High Throughput Imaging Echelle Spectrograph (HiTIES) [*Chakrabarti et al.*, 2001] at Tromsø, Norway, to obtain quantitative measurements of the electron and proton aurora. This spectrograph simultaneously observes four spectral windows selected at important auroral features: Balmer H_α and H_β for the proton aurora analysis (the focus of the present study) and N_2^+ 1NG (0,1) (427.8 nm) and OI 777.4 nm for the electron aurora analysis. This instrument offers a unique opportunity to address the issues raised by *Sigernes et al.* [1996] and to reinvestigate the Balmer decrement. A second spectrograph, the Proton Aurora Context (PAC) instrument, is used to provide qualitative information on the weather conditions and the overall auroral activity. Both instruments successfully operated over the winter-long campaigns from November 2001 to March 2002 and from October 2002 to April 2003. A comparison of the optical observations obtained during these campaigns with EISCAT radar measurements is discussed by *Galand et al.* [2003] (see http://www.unis.no/research/30AMProceedings.pdf). For all clear, near-new-moon nights with some auroral activity ($Kp > 1$), protons were always observed during some parts of the afternoon or evening. In this paper we first briefly describe both spectrographs and their calibration. Next, we present

the first data from both instruments for 20 January 2002. We discuss HiTIES observations in light of other measurements of H emission taken in twilight conditions. We compare the Balmer H emission profiles observed in proton aurora with earlier observations and with modeling results. Finally, we review our findings and argue on the relevance of using the Balmer decrement in proton aurora analysis.

2. Instrumentation

[7] Both PAC and HiTIES spectrographs were developed at the Center for Space Physics at Boston University (BU). They were set up at the EISCAT radar site in November 2001 and operated autonomously until April 2003. Data were transferred through internet and downloaded to BU regularly.

2.1. Proton Aurora Context Spectrograph

[8] The PAC instrument consists of an imaging spectrograph covering the $350-800$ nm spectral range. It is optically similar to the Coupling, Energetics and Dynamics
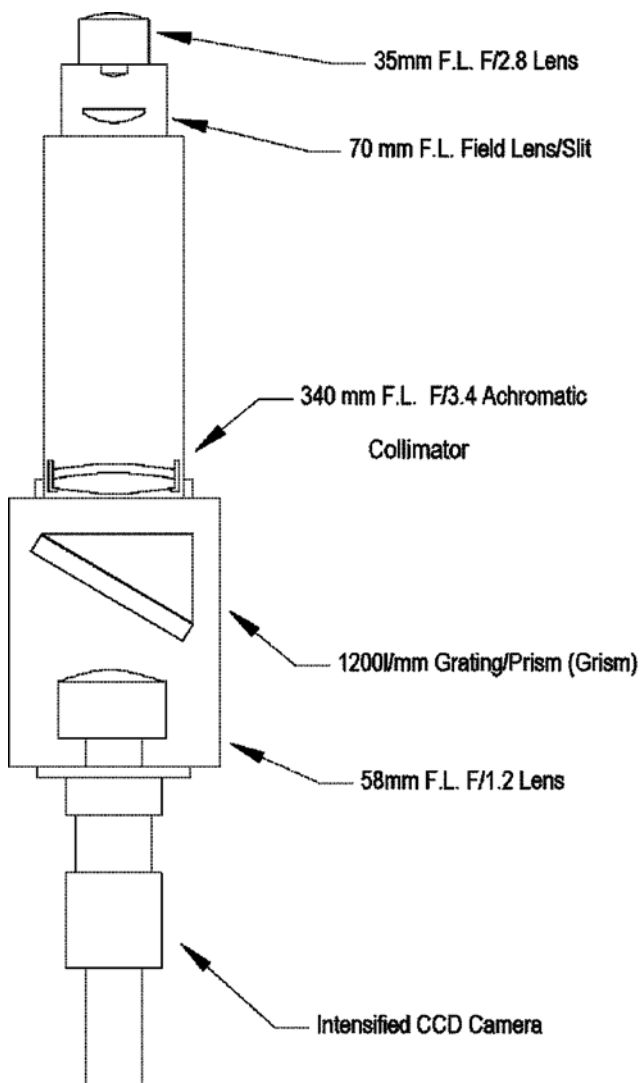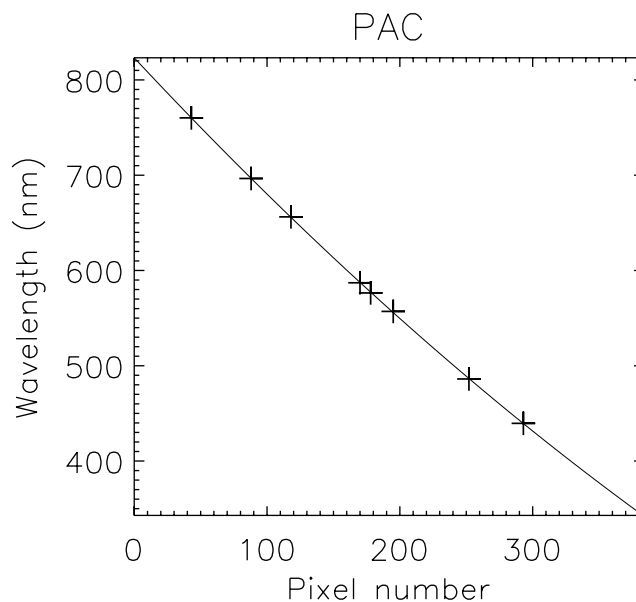

Figure 2. Wavelength calibration for PAC, using argon, hydrogen, krypton, and neon lamps. In a decreasing wavelength order the crosses correspond to Kr I (760.2 nm), Ar I (696.5 nm), H_α (656.3 nm), Kr I (587.1 nm), Ne I (576.4 nm), Kr I (557.0 nm), H_β (486.1 nm), and Ne I (439.6 nm). The solid line represents the fitting of a second-degree polynomial to the spectral lamp data.

of Atmospheric Regions (CEDAR) Optical Tomography Imaging Facility (COTIF) spectrographs, also built at BU [*Baumgardner et al.*, 1993]. The optical layout of the instrument is shown in Figure 1. It employs a grism and has a spectral dispersion of 1.2 nm pixel^{-1}, which is sufficient for a qualitative study on the state of the weather and the auroral activity. The $70°$ field of view is large enough to provide context information for the smaller field of view HiTIES observations. The PAC field of view was centered on the magnetic zenith (slanted $12.5°$ toward south). In order to determine the exact part of the sky probed by PAC, we identified astrophysical objects (stars, planets) on images taken during 2 clear nights (25 December 2001 and 20 January 2002). Since the azimuth and elevation angle of the astrophysical objects are precisely known, a correlation was established between the pixel number on the detector in the direction along the slit and the elevation angle using the time at which the object crossed PAC field of view. Note that the elevation angle is defined here as the distance from the southern horizon in degrees along the magnetic meridian. The exposure time was chosen to be 5 s to avoid saturation of the green and red lines. Sixteen images were co-added, so the total integration time was 80 s. Each saved image has a signal-to-noise ratio of ~ 60 for a 5 kR auroral line.

[9] Four spectral lamps (argon, hydrogen, krypton, and neon) were used for the wavelength calibration. The relation between the pixel number to the actual wavelength is obtained by fitting a second-degree polynomial to the reference wavelengths (Figure 2). No photometric processing is applied to the PAC data.

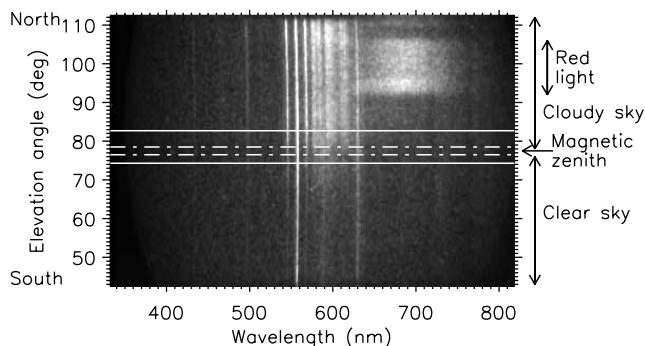[10] Before analyzing the HiTIES data we eliminated the days of bad weather (clouds, rain, snow) identified by

Figure 1. Schematic of Proton Aurora Context (PAC) spectrograph.

Figure 3. PAC image of the sky on 26 November 2001 at 0442 UT. The northern part of the sky is cloudy, whereas the southern part is clear. The horizontal solid lines show the field of view of HiTIES, which is centered on the magnetic zenith within 1°. The horizontal dash-dotted lines illustrate the elevation range used for deriving the PAC spectrogram shown in Figure 7. Note that the bright, rectangular spot in the red spectral range toward north (100° elevation) is due to light contamination from nearby red light-emitting diodes reflecting off the window.

PAC data. Figure 3 shows an image of the sky taken by PAC, which would be rejected for further analysis due to the presence of clouds in the field of view. The green (557.7 nm) and red (630.0 nm) airglow lines are prominent features spanning the whole field of view. A clear sky is seen in the southern part of the field of view, whereas the sky is cloudy in the northern part of the field of view. The latter is characterized by the presence of strong mercury and sodium lines around the green line, HgI 546.1 nm and the triplet NaI (568.263 nm, 568.819 nm, and 568.821 nm) as well as at HgI 435.8 nm and HgI 491.6 nm. These anthropogenic emissions (e.g., street lights) reach the PAC field of view through tropospheric scattering and can be used as an indicator of cloudiness. Another characteristic feature of a cloudy sky is the presence of an absorption around 589.3 nm (NaI 588.9 nm and NaI 589.6 nm). It is due to sodium broadband absorption in high-pressure sodium lights. The broadband red emission toward north is due to nearby light-emitting diode (LED) contamination reflecting on the window. It is located 10° away from the HiTIES field of view and thus does not affect the HiTIES data.

2.2. High Throughput Imaging Echelle Spectrograph (HiTIES)

[11] HiTIES is an imaging spectrograph capable of simultaneously observing multiple wavelengths in a wide spectral region from 390.0 to 770.0 nm [*Chakrabarti et al.*, 2001]. In this experiment the instrument was configured to record four selected wavelength regions in the vicinity of H_α (656.29 nm), H_β (486.13 nm), N_2^+ 1NG (0,1) (427.8 nm), and OI (777.4 nm). The intense N_2^+ and OI emissions, produced predominantly in electron aurora, were chosen because their excitation mechanisms and altitude range of production make them suitable for determining the energy of the incident electrons. The radiative lifetime of their excited state is sufficiently short so that collisional deactivation is minimal at auroral altitudes.

[12] HiTIES employs an Echelle grating, which is used at high orders and has a free spectral range of about 15 nm in a given order. In this experiment the order ranges from 24 for the OI line to 43 for N_2^+ 1NG 427.8 nm. Unlike conventional astronomical Echelle spectrographs, HiTIES uses a long input slit (45 mm) to increase its throughput. This instrument uses a "mosaic" of interference filters placed at the first image plane of the spectrograph to separate orders. Custom-made rectangular strips of interference filters are critically arranged to pass only the spectral information of interest. Light from other wavelengths of nearby orders is rejected by the filters. The spectrum is imaged onto a 1024×1024 charge-coupled device. The structure of HiTIES spectral images follow the arrangement of panels of the mosaic filter, which is illustrated in Figure 4. All the filter panels are rectangular in shape, except for the top one, which extends to the bottom of the image on the right side in order to increase the instrument sensitivity at OI 777.4 nm.

[13] The field of view of HiTIES can be changed from ~8° to 180° by changing the objective lens in front of the slit. For this campaign a 8.4° field of view, centered on the magnetic zenith, is used. The magnetic zenith profiles of H emissions yield well-defined upward and downward H atom components. The field of view and location are established by identifying astrophysical objects as they cross the slit.

[14] The wavelength calibration in the H_α and H_β windows is performed using neon and xenon lamps, respectively, in addition to a hydrogen lamp. The wavelength calibration obtained by fitting a second-degree polynomial to the spectral lamp data is shown in Figure 5. The dispersion in the H_α window is 0.042 nm pixel^{-1}, whereas it is 0.031 nm pixel^{-1} in the H_β window. The spectral resolution is obtained by fitting a gaussian to the spectral profile of the hydrogen lamp. The derived full width at half maximum (FWHM) is 0.10 nm for H_α and 0.06 nm for H_β. In this experiment the exposure time was chosen to be 4 min.

[15] With a similar instrument built at BU a group from the University of Southampton has successfully observed proton aurora in the nonsunlit atmosphere above Svalbard, Norway, in winter 2000 [*Lanchester et al.*, 2003]. A comparison of our observations with theirs is described in section 3.3. The daytime variant of the HiTIES instrument [*Pallamraju et al.*, 2002] has been successfully used to
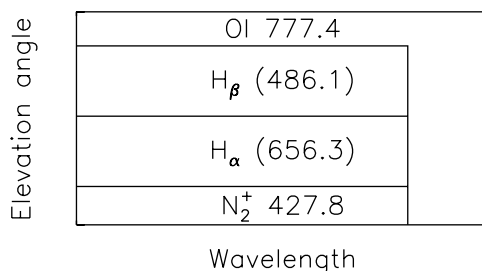

Figure 4. HiTIES image, representative of the panel arrangement of the mosaic filter in the image plane. The spatial information along the slit, which is oriented along the magnetic meridian, is converted to elevation angle (see Figure 3).
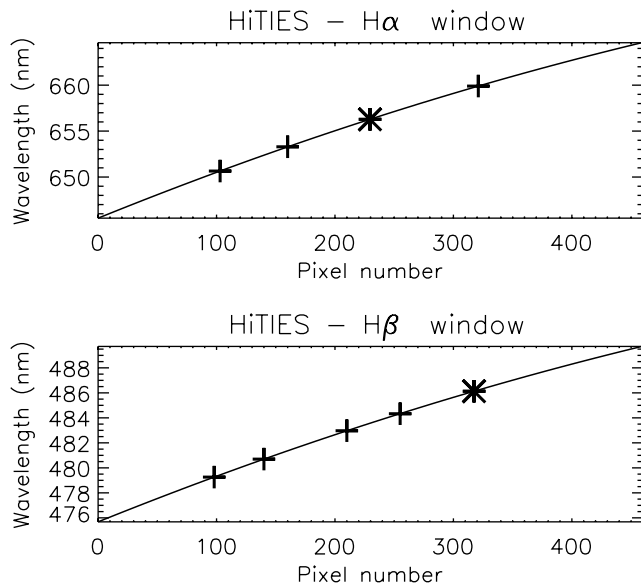
Figure 5. (top) Wavelength calibration for HiTIES H_α panel using a neon lamp (crosses) and a hydrogen lamp (asterisk). The neon lines are located at 650.65 nm, 656.28 nm, and 659.90 nm, and the H line (H_α) is located at 656.3 nm. (bottom) Wavelength calibration for HiTIES H_β panel using a xenon lamp (crosses) and a hydrogen lamp (asterisk). The xenon lines are located at 479.26 nm, 480.70 nm, 482.97 nm, and 484.33 nm, and the H line (H_β) is located at 486.1 nm. The solid lines represent the fitting of a second-degree polynomial to the spectral lamp data.

study OI (630.0 nm) emission from a sunlit aurora in conjunction with the Søndre Strømfjord incoherent scatter radar [*Pallamraju et al.*, 2001].

2.3. HiTIES Photometric Calibration

[16] Brightness calibration of HiTIES data was carried out using two different lamps. The first step was to take an image of our C^{14}-activated light source using a low-dispersion ($\sim$1 nm pixel^{-1}) spectrograph. The C^{14} source has a peak brightness of 1072 R nm^{-1} at 620 nm. This source has been calibrated a number of times in the last 15 years by different groups, with all of the measurements being within 20%. The output of this source falls off rapidly toward the blue, making it unsuitable for calibration at H_β spectral region. A second light source was built using a tungsten filament bulb. A reference image was obtained by imaging this secondary light source with the same spectrograph used for imaging the C^{14} source. This reference image was flat fielded using the C^{14} source image, and then the result was multiplied by the calibration curve for the C^{14} source. This provides a calibration curve for the tungsten source reliable for the wavelength range where the C^{14} source is brighter than 500 R nm^{-1}, i.e., between 575 and 680 nm.

[17] The emission characteristics of tungsten have been extensively studied. The deviation of this emission from a blackbody is known as the emissivity and is tabulated for various temperatures and wavelength regions. By plotting the emissivity-corrected blackbody curves (normalized at 620 nm) for various temperatures and choosing the one that has the same slope as that measured for the tungsten lamp, a

temperature of 3100 K is found (see Figure 6). The Planck curve for a 3100 K blackbody (corrected for emissivity) is then taken as our calibration curve for the tungsten source.

[18] Flat fields were taken on site in Norway using the tungsten source (care was taken to monitor the current flowing through the lamp so as to produce the same light output used during the lamp calibration). To calibrate a HiTIES spectrum, a sky spectrum is divided by these flats and then is multiplied by the calibration curve for the tungsten source to obtain a brightness in R nm^{-1}. Normalization by the tungsten source flat images removes any effect associated with vignetting.

3. Spectroscopic Analysis of 20 January 2002

3.1. Overview and Observing Conditions

[19] The evening of 20 January 2002 was very clear, with moderate auroral activity. The geomagnetic, planetary Kp index was equal to 3 in the 1500–1800 UT period and to 2 in the 1800–2400 UT period. The solar $f_{10.7}$ index was 222. An overview of the visible activity is shown in Figure 7. This spectrogram shows the PAC spectra extracted from the magnetic zenith from 1500 to 2300 UT. The data presented are raw data. The effect of sunlight is clearly seen until 1530 UT, with strong sodium doublet at 589.0 nm and 589.6 nm produced by resonant scattering of sunlight by the sodium atoms in the mesosphere. The sodium lines persist all through the night, albeit lower in brightness. The two vertical lines between 1530 and 1545 UT are from stars. The green line (OI 557.7 nm) and the red line (OI 630.0 nm) are present during the whole evening. These airglow lines had additional auroral contribution from 1815 UT onward. At
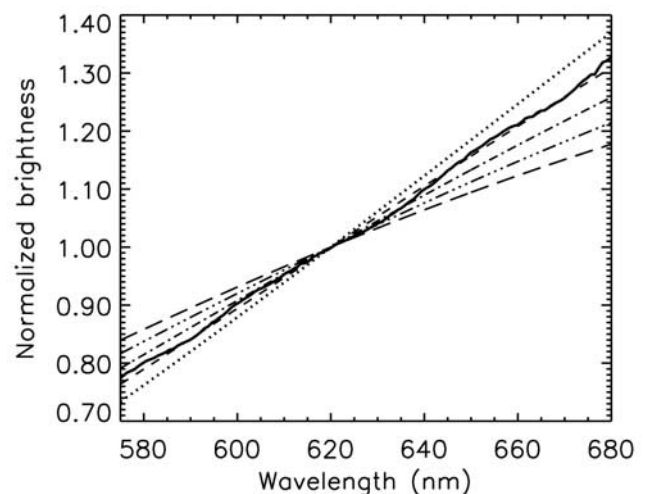

Figure 6. Observed and modeled tungsten spectra. The solid line represents the calibration curve for the tungsten lamp (derived from the C^{14} reference curve and the observed ratio between the tungsten lamp spectrum and the C^{14} source spectrum). The Planck curves corrected for the emissivity of Tungsten correspond to temperatures of 2900 K (dotted line), 3100 K (short-dashed line), 3300 K (dash-dotted line), 3500 K (dash-triple-dotted line), and 3700 K (long-dashed line). The different curves have been normalized to the photon flux at 620 nm. The better fit to the solid line is obtained for a temperature of 3100 K.
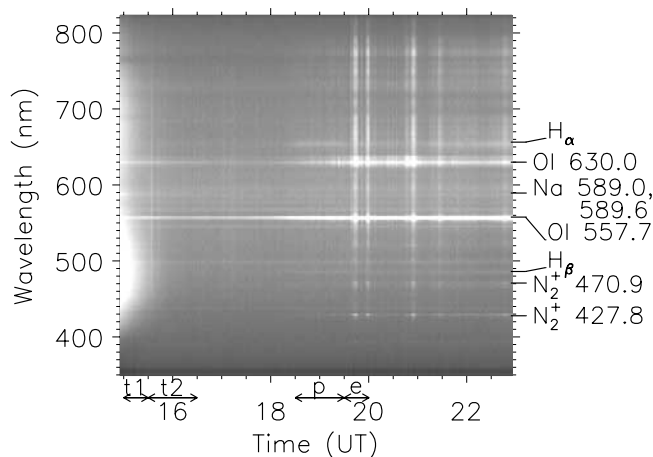
Figure 7. Spectrogram of the PAC data on 20 January 2002. The data are from the center of the field of view, as shown in Figure 3. The brightness is shown on a logarithm scale. The horizontal arrows identify four periods further studied with HiTIES data: "t1" (twilight from 1500 to 1528 UT), "t2" (later twilight from 1528 to 1625 UT), "p" (pure proton aurora from 1835 to 1932 UT), and "e" (proton aurora with strong electron arcs from 1937 to 2005 UT).

that time, H_α (656.3 nm) and H_β (486.1 nm) emissions intensify due to the presence of proton precipitation, which persists until 2300 UT. Intense electron arcs cross the field of view between 1930 and 2000 UT and around 2100 UT, 2130 UT, and 2245 UT. They are characterized by a large increase in N_2^+ 1NG emissions (470.9 nm, 427.8 nm, and 391.4 nm) and in N_2 1PG emissions longward of 600 nm. Sharp absorption features around 700 nm and 760 nm are due to water vapor and oxygen [*Curcio et al.*, 1964].

[20]   The keogram of the evening of 20 January 2002 in the vicinity of H_α is plotted in Figure 8. These raw data clearly show an enhancement of the brightness around 1815 UT, appearing first in the northern direction and propagating southward. The southward motion of proton aurora in the PAC field of view is corroborated by the IMAGE/FUV imager observations, which provide a global context to the ground-based observations. A set of images from SI12, which is sensitive to proton precipitations, clearly shows that Tromsø is located southward of the auroral oval in the afternoon (before 1730 UT) (H. Frey, personal communication, 2002). As the Earth rotates, Tromsø moves under the auroral oval; Tromsø is well within the proton aurora oval at 1830 UT. More detailed comparison between the PAC data and the IMAGE/SI12 observations is difficult due to the different spatial resolutions of the instruments and due to the uncertainties in the pointing of the SI12 instrument, yielding a registration error of ±200 km.

[21]   The intense features starting around 1930 UT in the H_α keogram, shown in Figure 8, are emissions from the electron arcs (seen in the spectrogram in Figure 7). The horizontal strip present in the north direction between 1900 and 2000 UT represents polaris. The large band located in the northern part of the field of view is due to LED pollution.

3.2.   High-Spectral-Resolution H Emission Profiles

[22]   The HiTIES data from 20 January 2002 are discussed in the present section 3.2 for different periods identified
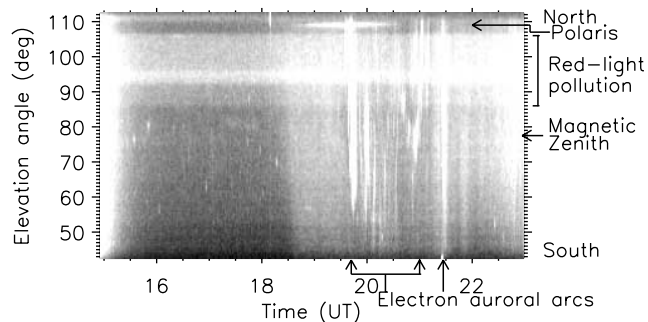

Figure 8.   Keogram of PAC data around H_α on 20 January 2002. The intensification starting around 1815 UT shows the presence of proton precipitation moving southward in the field of view. The large band covering the 86°–106° elevation range is due to the red light contamination also seen in Figure 3.

with horizontal arrows in Figure 7: twilight (t1), late twilight (t2), pure proton aurora (p), and proton aurora with electron arcs (e). The data related to the first two time periods, t1 and t2, are discussed in section 3.2.1, whereas the data associated with proton aurora are the focus of section 3.3.

3.2.1.   Galactic and Geocoronal Emissions

[23]   Figure 9 shows HiTIES data for H_α and H_β windows after the removal of the dark signal for the 1500–1528 UT twilight period (t1). This period corresponds to a solar depression angle between 9.5° and 11.6°.

[24]   Several absorption line features are clearly seen in the H_β panel in Figure 9. The brightness over the H_β panel is not uniform in the elevation direction, i.e., over space, because the data shown have not been corrected for vignetting. After correcting for this effect (by dividing by the flat image) we extract the H_β data and sum the emissions over the central 2° of the field of view. The derived spectrum, multiplied by the reference curve as explained in section 2.3, is plotted in Figure 10a. The locations of the H_β line and some FeI lines are shown with vertical solid and dash-dotted lines, respectively. These lines are solar Fraunhofer absorption features, which were compared with the high-resolution solar spectrum taken from Kitt Peak National Observatory to help provide wavelength calibration [*Kurucz et al.*,
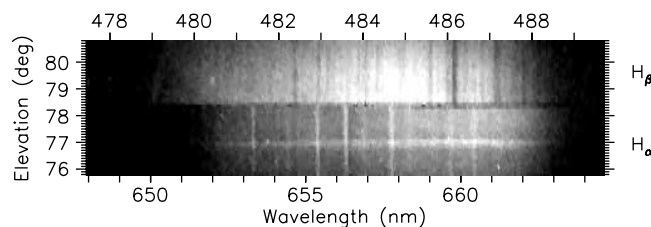

Figure 9.   HiTIES spectral image (associated with H_α and H_β panels) after dark count removal on 20 January 2002 between 1500 and 1528 UT. This period, corresponding to a solar depression angle between 9.5° and 11.6°, is labeled as the "t1" period in Figure 7 and illustrates twilight conditions. Only the H_α and H_β panels are shown as investigation of Balmer emissions is the focus of the present study.
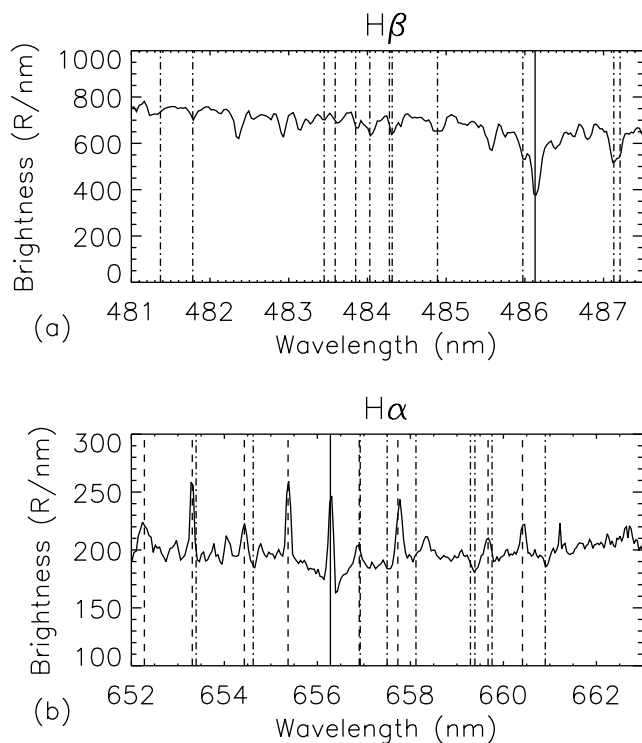
Figure 10. (a) Spectrum derived from the H$_\beta$ panel in Figure 9 ("t1" period). The vertical solid line corresponds to H$_\beta$ and the dash-dotted lines to FeI absorption lines. (b) Same as Figure 10a, but for H$_\alpha$. The vertical solid line corresponds to H$_\alpha$, the dashed lines to OH (6,1) emissions (P1(2)–P1(5) and P2(2)–P2(5)), and the dash-dotted lines to FeI absorption lines. The H$_\alpha$ emission is superimposed on a weak H$_\alpha$ Fraunhoffer absorption line.

Figure 12. (a) Spectrum derived from the H$_\beta$ panel in Figure 11 ("t2" period). The vertical solid line corresponds to H$_\beta$ and the dash-dotted lines to FeI absorption lines. (b) Same as Figure 12a, but for H$_\alpha$. The vertical solid line corresponds to H$_\alpha$, the dashed lines to OH (6,1) emissions (P1(2)–P1(5) and P2(2)–P2(5)).

1984]. The spectrum of Rayleigh-scattered sunlight decreases with depression angle up to the disappearance of sunlight effect, as it can be seen by comparing Figures 9 and 10a to Figures 11 and 12a.

[25] The H$_\alpha$ panel in Figure 9 shows fainter Fraunhofer absorption features compared with the H$_\beta$ panel. In the same manner as for H$_\beta$, a spectrum is derived for H$_\alpha$ for the 1500–1528 UT period (see Figure 10b). The position of the unshifted H$_\alpha$ line is shown with a vertical solid line. While during this twilight period H$_\beta$ is still entirely in absorption, the emission line in H$_\alpha$ is slightly larger than the absorption line. Faint absorption lines are located at FeI lines (vertical
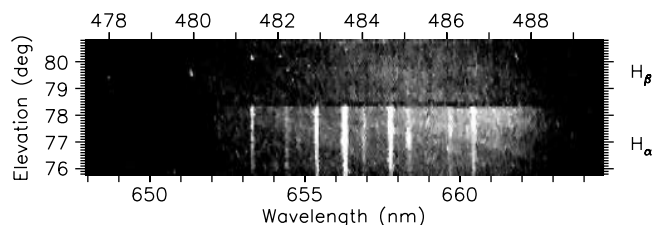

Figure 11. Same as Figure 9, but between 1528 and 1625 UT. This period, related to a solar depression angle between 11.6° and 16.2°, is labeled as the "t2" period in Figure 7 and corresponds to late twilight.
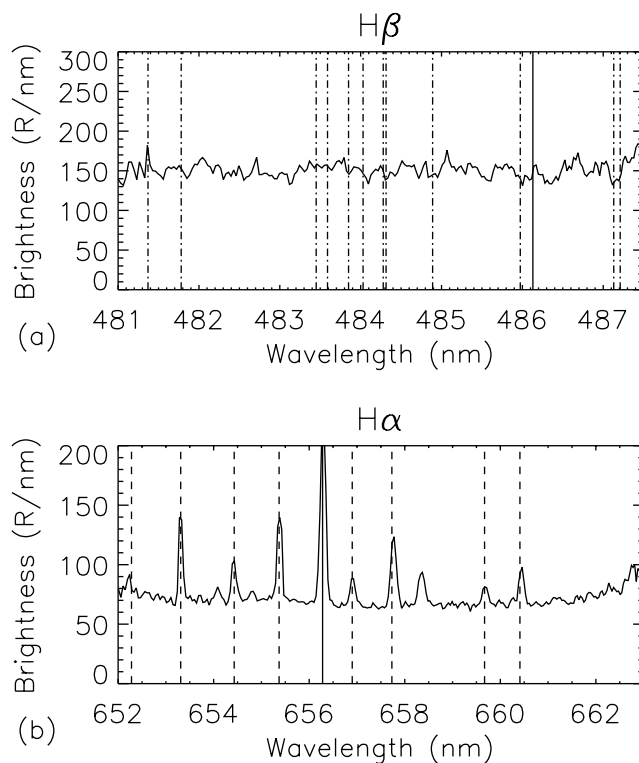
dash-dotted lines). The signal level associated with these Fraunhofer absorption features is smaller in the H$_\alpha$ spectral range compared to the H$_\beta$ range because the Rayleigh scattering is stronger in the blue than in the red.

[26] The spectrum plotted in Figure 10b shows strong OH airglow features (vertical dashed lines). These hydroxyl emissons are associated with the Meinel rotational lines from the P branch (P1(2)–P1(5) and P2(2)–P2(5)) of the OH(6,1) band. These lines originate at about 80–90 km in the mesosphere from the displacement reaction between H and O$_3$ [e.g., *Rees*, 1989]. The reduction of the contribution of sunlight with solar depression angle yields clear airglow signatures, as illustrated in Figure 12b for a solar depression angle ~14°. In addition to the OH bands, an emission feature is seen around 658.3 nm. It is most probably produced by NII of both airglow and nebular origin. Its brightness is a few Rayleighs.

[27] Finally, the spectra plotted in Figures 10b and 12b show an emission feature at H$_\alpha$ (vertical solid line). This H$_\alpha$ emission is produced from resonant fluorescence of sunlight H Lyβ (102.6 nm) by geocoronal H atoms [e.g., *Nossal et al.*, 2001]. H$_\alpha$ and H Lyβ lines share the same excited state H(n = 3). There is also an interstellar contribution produced by radiative recombination of ionized hydrogen gas with electrons [e.g., *Reynolds*, 1997] and a stellar contribution of chromospheric origin. These latter two contributions are labeled as "galactic" in the subsequent text. The narrow width of the observed H$_\alpha$ line in Figure 12b is essentially
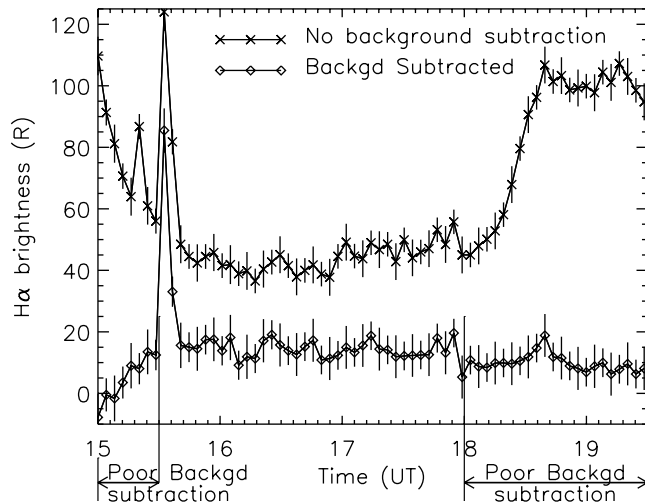
Figure 13. Time history of H_α brightness from HiTIES between 1500 and 1930 UT, including background (crosses) and with background subtracted (diamonds). The brightness was derived from the H_α panel of HiTIES from a spectral integration between 656.1 nm and 656.5 nm. The peaks that are left after background removal are from HII regions. The background subtraction is not suitable for time earlier than 1530 UT and later than 1800 UT (see text). The error bars are associated with the counting statistic. They represent the standard deviation ($\pm 1\sigma$). The systematic error in choosing the temperature for the light source (see section 2.3) is <3% between 2900 and 3300 K. The H_α brightness (with background subtracted) between 1600 and 1800 UT is of the order of 15 R, with a standard deviation of 5 R.

the instrument profile. Its FWHM of 0.17 nm is slightly larger than that observed with the hydrogen lamp (0.10 nm) due to the local standard of rest (LSR) velocities of the galactic sources and the velocities of the geocoronal H atoms. The HII region observed by the instrument shows maximum deviation of the LSR velocities from geocentric zero velocity of -25 km s^{-1} (after the Wisconsin H_α Mapper (WHAM) northern sky survey [*Haffner et al.*, 1999]), i.e., 0.055 nm red shift. The 0.1 nm spectral resolution of HiTIES does not allow the estimation of such LSR velocities and the separation of the galactic component from the geocoronal one. It should be noted that H_β is also produced by galactic and geocoronal sources, but its brightness is about 10 times smaller than H_α. It is not always as clearly identified as the H_α emission in our data. From Svalbard the unshifted H_β line is seen almost all the time [*Lanchester et al.*, 2003].

[28] The time history of H_α brightness from 1500 to 1930 UT is plotted in Figure 13. The brightness is derived from integrating the spectral profile between 656.1 and 656.5 nm. When no background is subtracted (solid line with crosses), a large decrease in brightness is seen from 1500 to 1530 UT. This decrease is associated with the increase of solar depression angle. Thus the solar contribution to the background through Rayleigh scattering and to the H_α emission from geocoronal contribution is reduced. The significant increase after 1800 UT is associated with the beginning of the proton aurora. The different peaks are

produced by the presence of stars (1520 UT, 1658 UT, 1701 UT, 1730 UT) or of HII regions (1533 UT, 1537 UT, 1605 UT, 1625 UT, 1629 UT, 1714 UT, 1747 UT, 1755 UT) in the field of view of the HiTIES instrument. The presence of a large number of HII regions is not surprising as the field of view of HiTIES crosses the Milky Way during this time period. We have checked that the different peaks are repeated on other days (e.g., 25 December 2001) after applying a 4 min d^{-1} shift associated with the Earth's orbital motion. The intense emission peaks at 1533 UT and 1537 UT are due to the HII region of the NGC 281 nebula. This result is corroborated by the WHAM northern sky survey providing the galactic H_α emission brightness [*Reynolds*, 1997; *Haffner et al.*, 1999]. A brightness enhancement is also seen at the same times in NII emissions at 658.3 nm and at 654.8 nm.

[29] The time history of H_α brightness obtained after removing the background is also shown in Figure 13 (solid line with diamonds). The background removal is applied by subtracting the signal near 656.1 nm and near 656.5 nm. The data before 1530 UT and after 1800 UT should be disregarded due to the presence of Fraunhofer absorption features (see Figure 10b) and to the presence of a broad H emission line produced in proton aurora (see section 3.3). The background removal allows the identification of the origin of the different peaks seen in the H_α history with background (shown with crosses in Figure 13). The stars have a continuum spectrum, whereas the HII regions are a source of H_α emission, yielding significant peaks even after the background removal.

[30] The H_α emission brightness is fairly constant (15 $\pm$ 5 R) between 1600 and 1800 UT (see Figure 13 (diamonds)). The shadow height varies from 325 km at 1600 UT up to 792 km at 1800 UT. *Kerr and Hecht* [1996] carried out high-latitude H_α observations from Søndre Strømfjord, measuring H_α brightness ranging between 12 and 14 R for a shadow height ranging from about 400 to 600 km, values which are consistent with our observations. The WHAM survey provides a galactic background in H_α between 8 and 11 R for the region of the sky seen by HiTIES between 1600 and 1800 UT. The field of view crossed the galactic equator near 1800 UT. At midlatitude, using WHAM, *Nossal et al.* [2001] estimated the geocoronal H_α brightness to be 9 R for 600–700 km shadow height altitudes during quiet solar conditions ($F_{10.7} = 70$). The larger solar activity on 20 January 2002 should not affect this value by more than 50% after midlatitude observations based on the two last solar cycles (S. Nossal, personal communication, 2003). However, no studies have yet been done over a full solar cycle in the high-latitude regions. The addition of the galactic background with the geocoronal contribution provides a brightness of 17–20 R. These values are again consistent with our measurements (Figure 13).

3.2.2. Proton Aurora

[31] The intensification of H_α and fainter H_β seen in PAC from 1815 UT (see Figure 7) is associated with the appearance of broad, Doppler-shifted H_α and H_β emissions, as illustrated in Figure 14. Such profiles are a unique signature of proton precipitation into the atmosphere.

[32] H_α and H_β spectra are extracted from Figure 14 in the same way as for Figure 10. The results are shown in Figure 15. The H_β profile has a complicated structure
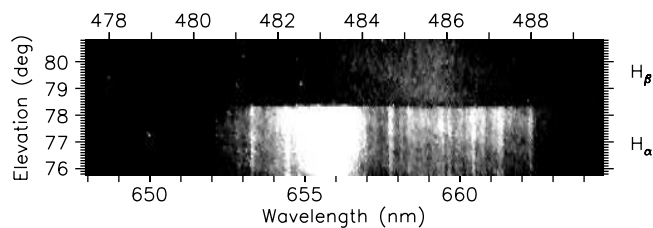
Figure 14. Same as Figure 9, but between 1836 and 1932 UT. This period, characterized by the presence of proton precipitation, is labeled as the "p" period in Figure 7. The solar depression angle is around 30°.

induced by the low signal-to-noise ratio (>25% for the electron counting statistics near the peak) along with the blending of weak atmospheric emission lines. As a result, the signal is framed by two extreme curves (thin dotted lines in Figure 15a), within which the "true" Doppler-shifted profile lies. The thick dotted line represents the average between these two extreme profiles. In order to check the validity of our method, we have plotted the difference between the observed profile (solid line in Figure 15a) and the estimated Doppler-shifted profile (thick dotted line in Figure 15a). This difference, shown in Figure 16a, does not exhibit any residual of the broad Doppler-shifted profile. Some of the peaks are associated with the low signal-to-noise, while others, identified with a vertical arrow, are persistent over time. In addition to the unshifted H_β line of galactic and geocoronal origin, the persistent peaks are seen during other nights, mostly during strong electron arcs, and are probably from the N_2 Vegard-Kaplan (2,15) emission band. The spectral location of the band head of this emission is indicated with the vertical dash-triple-dotted line. The large excursion seen around 482.5 nm is diregarded in our estimation of the Doppler-shifted H_β. It is the result of a defect in the chip and constitutes an unrecoverable flat field error. The total brightness of the decontaminated Doppler-shifted H_β profile (thick dotted line in Figure 15) is found to be 155 R, which is consistent with previous observations [e.g., *Eather*, 1967; *Søraas et al.*, 1974].

[33] The Doppler-shifted H_α profile is contaminated by airglow emissions from OH (6,1) bands (dashed lines), by geocoronal and galactic H emissions (solid line), and by auroral emissions (dash-triple-dotted lines). The strongest auroral features are N_2 1PG (7,4) and (6,3) emissions at 654.5 nm and at 662.4 nm, respectively. Owing to the high spectral resolution of HiTIES, all these contaminating emissions are clearly resolved in the spectrum. As the signal-to-noise ratio for H_α is better than for H_β and the contaminated lines are easily identified, our approach to assess the decontaminated Doppler-shifted H_α profile is different from that applied for H_β. The subtraction of the unshifted H_α line contamination is performed by using the galactic and geocoronal H_α profile observed during late twilight, before the proton aurora starts. The brightness of the line is scaled to the maximum of the brightness observed at H_α (656.3 nm) during the proton aurora after having removed the background derived from both sides of the line. This technique is independent of the brightness of the twilight H_α. As the hydroxyl rotational temperature changes over time, the ratio between different OH emissions varies,

and the method used for H_α cannot be applied to the OH bands. Therefore we fit the blue-shifted wing of the Doppler profile observed in the proton aurora by a smooth curve such that the difference between the observed profile and the assessed curve has a straight baseline and is comparable to the longward side of the profile (>658 nm) not affected by the H Doppler-shifted profile. The resulting decontaminated profile is shown with the dotted line in Figure 15b and is associated with a total brightness of 375 R. The difference between the observed profile and the assessed Doppler-shifted profile is shown in Figure 16b in solid line. The major peaks are associated with the airglow, auroral, and galactic/geocoronal lines from OH band, N_2 1PG band, and H_α, identified by dashed lines, dash-triple-dotted lines, and the solid line, respectively. The offset seen over the
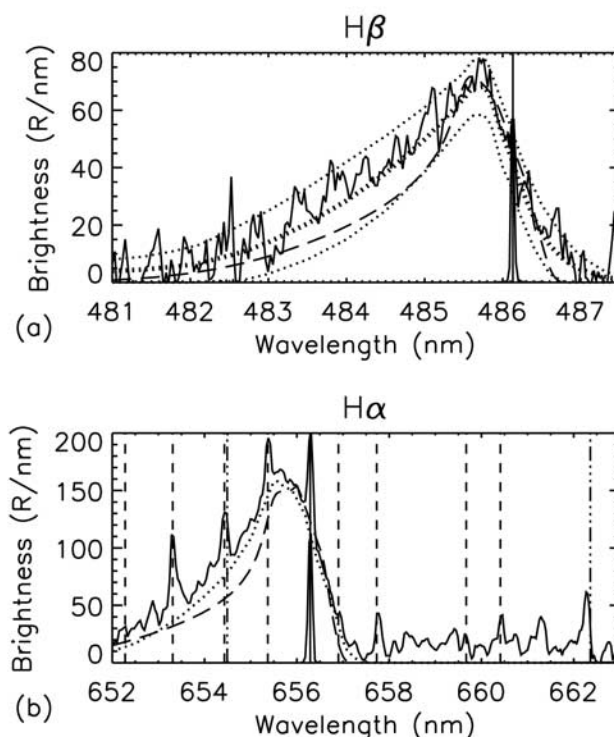

Figure 15. (a) Spectrum derived from the H_β panel in Figure 14 ("p" period). The vertical solid line corresponds to H_β. The H lamp spectrum has been overplotted for reference (narrow line near H_β). The observed profile is framed between two extreme curves (thin dotted lines), within which the "true" Doppler-shifted H_β profile lies. The decontaminated Doppler-shifted H_β profile, average of the two extreme profiles, is shown as a thick dotted line. The smooth dashed line corresponds to the magnetic zenith Doppler H_β profile provided by the proton transport model, assuming an isotropic incident proton flux with a Maxwellian distribution in energy and a mean energy of 40 keV. (b) Same as Figure 15a, but for H_α. The vertical solid line corresponds to H_α, the dashed lines to OH (6,1) emissions (P1(2)−P1(5) and P2(2)−P2(5)), and the dash-triple-dotted lines to auroral N_2 1PG (7,4) (654.5 nm) and (6,3) (662.4 nm) emissions. The decontaminated Doppler-shifted H_α profile is shown as a thick dotted line. The H lamp spectrum has been overplotted for reference (narrow line near H_α).
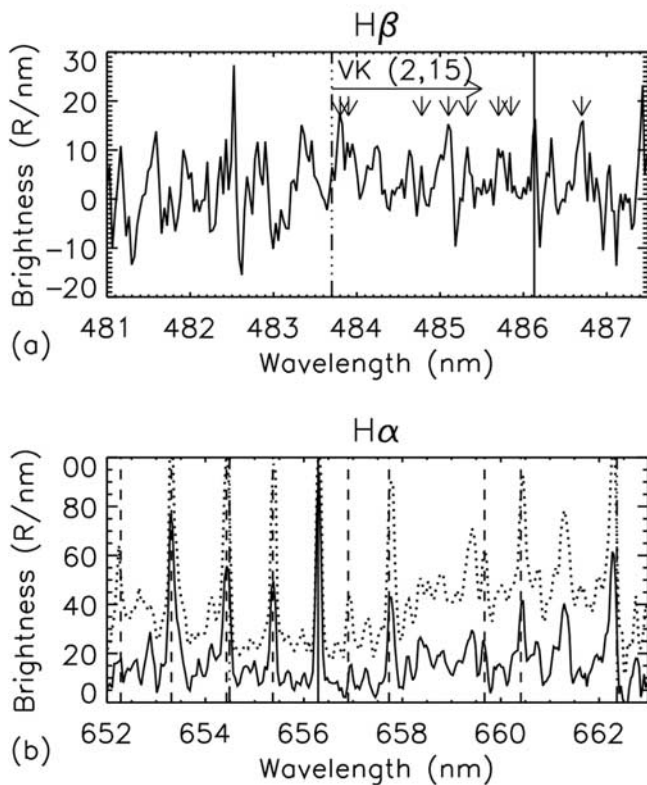
Figure 16. (a) Difference between the H_β profile observed during the "p" period (solid line in Figure 15) and the decontaminated profile (thick dotted line in Figure 15). The vertical solid line corresponds to H_β and the vertical dash-triple-dotted line to the band head of the N_2 Vegard-Kaplan (2,15) band. The vertical arrows identify peaks that are persistent and seen in strong electron arcs. (b) Same as Figure 16b, but for H_α. The vertical solid line corresponds to H_α, the dashed lines to OH (6,1) emissions (P1(2)−P1(5) and P2(2)−P2(5)), and the dash-triple-dotted lines to auroral N_2 1PG (7,4) (654.5 nm) and (6,3) (662.4 nm) emissions. The spectrum acquired during diffuse pure electron aurora around 0500 UT on 26 December 2001 is shown as a dotted line. Its offset is arbitrary.

whole spectral range is the result of unresolved spectral lines. As an example of the validity of the technique, this profile compares favorably with a spectrum obtained during diffuse electron aurora, when no proton precipitation was occurring (dotted line in Figure 16b). The latter was acquired around 0500 UT on 26 December 2001, and its offset is arbitrarily chosen for the purpose of comparison.

[34] For comparison with the decontaminated profiles, modeled magnetic zenith H profiles obtained with an incident proton flux of 40 keV mean energy are overplotted in Figure 15. The simulations are based on the proton transport model described by *Galand et al.* [1997]. The cross section set is that described by *Lanchester et al.* [2003]. Collisional angular redistribution is included for energies below 1 keV. The neutral atmosphere (N_2, O_2, and O) adopted is specified by the Mass Spectrometer and Incoherent Scatter model (MSIS-90) [*Hedin*, 1991] for the location of Tromsø on 20 January 2002 at 1900 UT for a magnetic activity of $A_p = 7$ and a solar index of $f_{10.7} = 222 \times 10^{-22}$ Wm^{-2} Hz^{-1}. The incident proton flux is

assumed to be isotropic over the downward hemisphere and to have a Maxwellian distribution in energy. The energy flux is normalized to 1 mW m^{-2}. The synthetic Doppler profiles are convolved with an instrument function of 0.06 nm FWHM for H_β and 0.10 nm FWHM for H_α in agreement with measured HiTIES instrument function. The synthetic spectrum is scaled to achieve an approximate match to the decontaminated spectrum. As the energy flux is directly proportional to the Doppler profile, this fit provides an estimate of the energy flux associated with the observed spectrum. The computation of the Doppler profile takes into account atmospheric transmission. On the basis of a radiative transfer equation, *Stamnes and Witt* [1985] derived the transmission of emitted radiation in the upper atmosphere and observed from the ground. Their computation includes atmospheric Rayleigh scattering, absorption by ozone, and ground albedo. From this work, assuming a ground albedo of 0.8, a polar angle of $-12.5°$, and clear-sky conditions, we derive a transmission value (including scattering in and out the field of view) of 94.2% for H_β and of 98.7% for H_α.

[35] The Doppler-shifted magnetic zenith H profiles result from excited H atoms inside the energetic proton beam. The profiles are blue-shifted as most of the energetic H atoms are moving downward toward the observer. The violet wing, shortward of the blue-shifted peak, is sensitive to the mean energy of the incident protons [*Lummerzheim and Galand*, 2001]. Our simulations show that a mean energy of 40 keV provides a good fit to the observed violet wings. The magnetic zenith H profiles observed by HiTIES have a red-shifted wing. This wing has a half width at half maximum about 10 times greater than the instrument resolution. To illustrate this, the H lamp profile is overplotted in Figures 15a and 15b, which demonstrates the physical nature of the red wing seen in auroral Balmer profiles. The red wing observed in proton aurora results from the upward H atom flux produced by collisional angular redistribution inside the proton beam, as predicted by modeling [*Galand et al.*, 1998]. The shapes of the modeled and observed red wings of the H profiles are in good agreement. The influence of scattering on the profile shape is discussed in section 4.

[36] Scaling the modeled H_β spectrum to the observed one yields an incident energy flux of 0.7 mW m^{-2}, whereas scaling the modeled H_α spectrum to the observed spectrum yields an incident energy flux of 0.4 mW m^{-2}. The difference in energy flux values found between the H_α and the H_β scaling could be explained by the discrepancy between the measured and modeled Balmer decrements, a quantity which is discussed at length in section 4. The derived values for the energy flux are in agreement with the Air Force Research Laboratory's auroral statistical model derived from the polar-orbiting DMSP particle data [*Hardy et al.*, 1989]. This statistical model predicts a value of 0.4 mW m^{-2} for the location of Tromsø at 1900 UT for moderate magnetic conditions. If the shapes of the synthetic profiles (dashed lines) agree overall with those of the observed Doppler-shifted profiles (thick dotted lines), the model provides low values for part of the violet wing around 484−485 nm for H_β and 654−655 nm for H_α. This underestimation of the synthetic profiles compared to the observed profiles may be explained by the uncertainties on

Table 1. Comparison of the Characteristics of the H_β Doppler-Shifted Profiles Observed in Proton Aurora From Different Locations and Instruments

Location	Magnetic Latitude, deg	Time Sector	Spectral Resolution, nm	Wavelength Peak, nm	Half-Width (Violet Wing), nm	Half-Width (Red Wing), nm
Tromsø, Norway	66.4	afternoon to night	0.06	485.75	1.45	0.50
Poker Flat, Alaska	65.2	afternoon to night	0.43	485.8	1.2–2.0	0.5–0.7
Svalbard, Norway	75.0	dayside	0.13	485.9	0.6–0.8	0.5–0.7

the H emission cross sections of energetic H^+ and H impact on the atmospheric constituents and by the uncertainties on the energy distribution of the incident protons, chosen to be Maxwellian in our simulations. Coincident space-based particle measurements at low altitudes (600–1000 km) would be needed to further constrain the brightness validation and the particle characteristics derivation. Unfortunately, none were available between 1800 and 2300 UT over Tromsø.

[37] Characteristics of H_β Doppler-shifted profiles observed at Tromsø (present study, Figure 15a), at Poker Flat [*Lummerzheim and Galand*, 2001], and at Svalbard [*Lanchester et al.*, 2003] are presented in Table 1. Given the different spectral resolutions of the instruments and the different dates, the wavelength of the peak and the half-width of the red wing are similar at the three sites. However, the half-width of the violet wing is smaller at Svalbard compared with those measured at Tromsø and Poker Flat. Note that during an unusual, bright proton aurora event at Svalbard the half-width of the violet wing reached larger values than 0.8 nm [*Lanchester et al.*, 2003]. Tromsø and Poker Flat, located at similar magnetic latitudes, observe the central plasma sheet population precipitating in the evening sector, whereas Svalbard, located at a higher magnetic latitude, observes softer precipitation from the dayside. Modeling [*Galand et al.*, 1998] shows that (1) the spectral extent of the violet wing is sensitive to the energy of the incident particles and therefore is expected to be smaller at polar sites at dayside compared to more equatorward sites in the evening sector; (2) at high spectral resolution the wavelength of the peak is not significantly sensitive to the hardness of the precipitation, yielding similar Doppler shifts at different locations; and (3) the red wing is induced by collisional angular redistribution that acts mainly at low energies, making the half-width of the red wing weakly dependent on the energy of the incident protons.

[38] During intense electron arcs, all auroral features are strongly enhanced. Figure 17 presents the HiTIES data for the 1937–2005 UT period. The N_2 1PG bands in the H_α panel are significantly intensified. The OI 777.4 nm and N_2^+ 427.8 nm panels also show intensification of the oxygen lines and N_2^+ 1NG bands. The presence of these intense electron arcs in the field of view of HiTIES offers the possibility of analyzing the auroral emissions in terms of electron aurora, similar to the study described by *Lummerzheim et al.* [1990]. This is left for a future publication.

4. Discussion and Conclusions

[39] In this paper we have demonstrated the capabilities of PAC and HiTIES instruments for the study of twilight and auroral activity, in particular during proton precipitation. The wavelength calibration was successfully validated

through the Fraunhofer absorption lines and airglow features. The field of view of the instruments was confirmed to be centered around the magnetic zenith through the identification of stars and planets crossing the field of view.

[40] During the absence of proton aurora, our brightness measurements of H_α emissions are consistent with previous observations, as discussed in section 3.2.1. Such nonauroral emissions are primarily of galactic and geocoronal origin. The H_α geocoronal contribution and its variability have been widely observed and discussed at low latitude [e.g., *Kerr et al.*, 2001a, 2001b] and at midlatitude [e.g., *Nossal et al.*, 2001, and references therein]. However, only a few observations have been carried out in high-latitude regions. Our technique, applied at twilight time, could be used to observe the variability of the geocoronal component over time and to compare the derived variability with midlatitude sites. It should be noted that the most suitable conditions would be for viewing outside the Milky Way, which provides a large background of the same order as the geocoronal background for shadow height of the order of 600 km.

[41] The Doppler-shifted H_β profile observed in proton aurora (see Figure 15a) is in agreement with modeling results [*Galand et al.*, 1998] and with earlier ground-based observations [*Lummerzheim and Galand*, 2001; *Lanchester et al.*, 2003]. The high spectral resolution of HiTIES allows us to use H_α for proton aurora study because we are able to clearly identify the blended airglow and aurora lines in the profile. Comparison of the observed H_α spectrum with modeled profiles inferred from coincident space-based particle measurements at low altitudes is the next step to further constrain the validation of the H_α analysis.

[42] The simultaneous observations of H_α and H_β at high spectral resolution by the same instrument provide an unprecedented opportunity to investigate the Balmer decrement. This decrement has been under debate for several decades due to discrepancies between observations and modeling [e.g., *Sigernes et al.*, 1994b]. Since it has been predicted to be, in principle, dependent on the mean energy of the incoming protons, it could potentially be of great
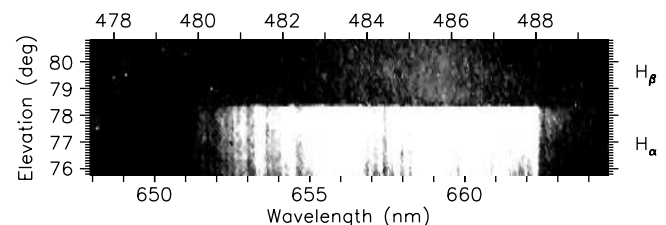

Figure 17. Same as Figure 9, but between 1937 and 2005 UT. This period, characterized by the presence of proton aurora and intense electron arcs, is labeled as "e" in Figure 7.

Table 2. Uncertainties on the Estimation of the H_α and H_β Brightnesses and Largest Possible Error in the Balmer Decrement During the Proton Aurora Studied in Figure 15[a]

Uncertainties Associated With	H_α, %	H_β, %	Balmer Decrement, %
Calibration (systematic error) (±200 K uncertainty on the blackbody temperature)	3	13	18
Atmospheric scattering (maximum scattering into the field of view for clear sky conditions)	5	10	17
Estimation of continuum background	10	20	38
Estimation of the area of the profile due to noise and contamination (spectral background)	10	35	69

[a]It should be noted that the error in the Balmer decrement for each of the sources of error identified is the ratio of the extreme H_α to H_β estimates. It is a conservative approach, providing larger errors than the statistical one using root-mean-square.

interest in the analysis of proton aurora. Figures 14–17 show that the Doppler-shifted H Balmer profiles in proton aurora are contaminated by auroral and airglow emissions. By including the lines blended in the proton-induced Doppler-shifted profile, a Balmer decrement of 2.8 is derived from Figure 15. By removing the contaminating lines from the Doppler-shifted H profiles (as explained in section 3.3), the Balmer decrement decreases by 14%, reaching a value of 2.4. This emphasizes the importance of making high-spectral-resolution observations in order to be able to estimate the "true" Balmer decrement associated with the proton aurora.

[43] Our measured Balmer decrement is sensitive to various sources of uncertainties, which are gathered in Table 2. The brightness calibration was done with a Tungsten white light source with a Planck temperature of 3100 K. If we consider a temperature 200 K away from 3100 K, the H_α brightness is not significantly affected with a variation <3%. The effect on H_β brightness is larger, up to 13%, as H_β is further away from 620.0 nm than H_α (see Figure 6). The Balmer decrement is 2.83 and 2.06 for a temperature of 2900 K and 3300 K, respectively. The uncertainties in the choice of the temperature for the photometric calibration yields an uncertainty in the Balmer decrement of ±15–20%. Another source of uncertainty is the atmospheric scattering. There is extinction due to scattering out of the field of view and contamination from scattering into the field of view. We applied transmission coefficients to the modeling results in order to compare with the observed Balmer decrement. The contamination of the brightness by proton aurora scattering into the field of view is assessed to be <5% for H_α and <10% for H_β [Bernstein et al., 2002]. These values yield a maximum error on the Balmer decrement of <17%. Eather and Jacka [1966] estimated the atmospheric scattering to have an even smaller effect. Their observations showed that scattering from one part of the sky illuminated by aurora to the other part not undergoing particle precipitation is <1%. It is difficult, however, to estimate the scattering into the field of view as it is a function of the covering of the sky by proton aurora and of the sky conditions. At the time the H profiles were observed the whole PAC field of view was filled with proton aurora. In addition, the anthropogenic mercury emissions reaching the PAC field of view through tropospheric scattering on clouds were weak, indicating conditions of clear sky. Another source of uncertainty is related to the estimation of the continuum background. The choice for the baseline above which the brightness will be estimated is assessed to be ~10% for H_α and ~20% for H_β, yielding an error of up to 40% on the Balmer decrement. Finally, the estimation of the shape of the profile due to noise and contamination by spectral lines affects the estimation of the

proton-induced H brightness. For H_α this uncertainty is evaluated to be <10%. For H_β the uncertainty, derived from the profiles framing the observations (thin dotted lines in Figure 15a), is 35%. The low signal to noise level for H_β greatly affects the estimate of the H_β brightness, yielding an error on the Balmer decrement of up to 70%.

[44] Eather [1967] reported measured values of the Balmer decrement from 1 to 7. This large range of values was attributed to the variation of photographic plate or photomultiplier sensitivity with wavelength, the low absolute brightness involved, and the contamination from overlapping emissions of airglow, galactic, and auroral origin (see section 3.3). The latter varies with the presence and characteristics of electron aurora, as illustrated in Figure 17. Using a spectrometer for H_α and a meridian scanning photometer for H_β from dayside at Svalbard, Sigernes et al. [1996] obtained a Balmer decrement between 4.5 and 9.5 after removal of the OH emission lines from the H_α profile. These values, larger than our results, may be explained by the narrowness (0.7 nm) of the bandpass of the H_β filter, yielding an underestimation of the H_β brightness. In addition, as discussed below, the dayside proton aurora is usually induced by lower-energy particles than those observed at the evening side at Tromsø [e.g., Hardy et al., 1989], yielding a larger Balmer decrement.

[45] The Balmer decrement has also been estimated through modeling [e.g., Eather, 1967; Rees, 1982; Van Zyl et al., 1984; Srivastava and Singh, 1987; Sigernes et al., 1994b]. These researchers all found that the Balmer decrement decreases with the mean energy, E_m, of the incoming protons. One exception comes from the study by Rees [1982] and can be explained by the choice in the energy deposition function [Basu et al., 1987]. For E_m between 0.1 and 40 keV the values for the Balmer decrement range from 4.4 to 6 after Van Zyl et al. [1984], from 5.6 to 6 after Srivastava and Singh [1987], and from 6.2 to 9 after Sigernes et al. [1994b]. The discrepancies in the results can be attributed to the intrinsic assumptions inherent in the different approaches using average energy loss or a semi-empirical range relation. All these studies appeal to the same Balmer emission cross section set of H^+/H impact on N_2 and O_2 proposed by Van Zyl et al. [1984], which provides cross section values to 3 keV only. No extended work has been reported on the Balmer cross section of O. Differences in the extrapolation at higher energies can largely account for discrepancies in the estimated Balmer decrement. In all these modeling studies, atmospheric absorption and scattering is neglected.

[46] In order to investigate further the reason for this discrepancy, we appeal to the comprehensive proton transport model described in section 3.3 and compute the Balmer

GALAND ET AL.: PROTON AURORA AT TROMSØ

decrement for the location at Tromsø under different auroral conditions (Kp = 2 and 4). For the Balmer emission cross section we use those proposed by *Strickland et al.* [1993]. These authors pointed out that the estimation of the H$_\beta$ emission cross section due to proton and H atom impact on N$_2$ and O$_2$ above 3 keV is very uncertain. The Balmer α and β cross sections on O are assumed to be 0.7 of those on O$_2$. We obtain a Balmer decrement decreasing with energies, with values between 4.4 and 5.0 for proton mean energy ranging from 5 to 40 keV. No significant differences were found in the Balmer decrement between Kp = 2 and Kp = 4 cases. When including the collisional angular redistribution in the model [*Galand et al.*, 1998], the Balmer decrement decreases only by about 2%. Applying transmission values of 94.2% for H$_\beta$ and of 98.7% for H$_\alpha$ to the Balmer brightnesses, as explained in section 3.3, yields an increase of 5% of the Balmer decrement. The derived values range from 4.6 to 5.2 over the 5–40 keV proton mean energy.

[47] Bearing in mind the large uncertainties in the collision cross section, the modeled values we derived for the Balmer decrement are close to those obtained in the three previous studies described above. All the modeling Balmer decrement values are, however, larger than the 2.4 Balmer decrement we observed over Tromsø on 20 January 2002. The discrepancy found between our modeling work and the observations may be explained by different factors. In addition to the uncertainties on the data discussed earlier in this section (see Table 2), the modeling approach is strongly limited by the uncertainties on the Balmer emission cross section set by energetic proton and H atom impact on N$_2$, O$_2$, and O. Reactions producing hydrogen atoms in excited states could have cross sections for atomic oxygen targets that are quite different from N$_2$ and O$_2$ targets, favoring production of (n = 4) H atoms over (n = 3) atoms. The effect would have to be large, however, if it is to significantly alter the Balmer decrement since most of the emission originates in the molecular-dominated region of the atmosphere [*Rees*, 1982]. *Van Zyl and Neumann* [1980] have discussed how collisional deactivation of fast H atoms in the relatively long-lived 3s and 4s states could decrease the expected H$_\alpha$ and H$_\beta$ emissions during hard proton aurora occurring at low altitudes. The estimate of the collisional frequency for deactivation at 10 keV by N$_2$ impact shows that the quenching should not play a significant role above 100 km. Contribution from nearby proton aurora may also influence the magnetic zenith Doppler shape as well as the Balmer decrement. The accurate assessment of such a contribution requires comprehensive radiative transfer calculations, including scattering of proton aurora Doppler profiles into the field of view. However, such a calculation has not yet been done. Until then, we can only rely on observations, which tend to show that such a contribution is expected to be small [*Eather and Jacka*, 1966]. To conclude, we would like to emphasize that the large range of Balmer decrement measurements reported in the literature and by us vitiates its use for characterizing the auroral proton flux. Numerous uncertainties in measured and modeled H$_\alpha$ and H$_\beta$ line profiles preclude using the Balmer decrement as an indicator of the mean energy of the incident protons. This result is reinforced by recent modeling studies, which find a smaller dependence of the decrement on energy than originally thought [e.g., *Srivastava and Singh*, 1987; *Sigernes et al.*, 1994b] (present study). The violet wing [*Lummerzheim and Galand*, 2001; *Lanchester et al.*, 2003], rather than the Balmer decrement, is a more suitable indicator of the mean energy of the proton precipitation flux.

[48] For a better assessment of the proton characteristics from the H Balmer profiles, there is a crucial need for more accurate Balmer emission cross sections of H$^+$/H impact on the atmospheric species, in particular for H$_\beta$ above 3 keV or on O. When the H line analysis in proton aurora is well established and validated from ground, it will be a powerful tool for the assessment of the particle energy input over larger regions of the auroral oval from a space-based platform.

References

Basu, B., J. R. Jasperse, R. M. Robinson, R. R. Vondrak, and D. S. Evans (1987), Linear transport theory of auroral proton precipitation: A comparison with observations, *J. Geophys. Res.*, *92*, 5920–5932.

Baumgardner, J., B. Flynn, and M. Mendillo (1993), Monochromatic imaging instrumentation for applications in aeronomy of the Earth and planets, *Opt. Eng.*, *32*, 3028–3032.

Bernstein, R. A., W. L. Freedman, and B. F. Madore (2002), The first detections of the extragalactic background light at 3000, 5500, and 8000Å (II): Measurement of foreground zodiacal light, *Astrophys. J.*, *571*, 85–106.

Chakrabarti, S., D. Pallamraju, J. Baumgardner, and J. Vaillancourt (2001), HiTIES: A High Throughput Imaging Echelle Spectrograph for ground-based visible airglow and auroral studies, *J. Geophys. Res.*, *106*, 30,337–30,348.

Curcio, J. A., L. F. Drummeter, and G. L. Knestrick (1964), An atlas of the absorption spectrum of the lower atmosphere from 5400 A to 8520 A, *Appl. Opt.*, *3*, 1401–1409.

Deehr, C., and D. Lummerzheim (2001), Ground-based optical observations of hydrogen emission in the auroral substorm, *J. Geophys. Res.*, *106*, 33–44.

Deehr, C. S., D. A. Lorentzen, F. Sigernes, and R. W. Smith (1998), Dayside auroral hydrogen emission as an aeronomic signature of magnetospheric boundary layer processes, *Geophys. Res. Lett.*, *25*, 2111–2114.

Eather, R. H. (1967), Auroral proton precipitation and hydrogen emissions, *Rev. Geophys.*, *5*, 207–285.

Eather, R. H., and F. Jacka (1966), Auroral hydrogen emission, *Aust. J. Phys.*, *19*, 241–274.

Frey, H. U., S. B. Mende, C. W. Carlson, J.-C. Gérard, B. Hubert, J. Spann, R. Gladstone, and T. J. Immel (2001), The electron and proton aurora as seen by IMAGE-FUV and FAST, *Geophys. Res. Lett.*, *28*, 1135–1138.

Galand, M., J. Lilensten, W. Kofman, and R. B. Sidje (1997), Proton transport model in the ionosphere: 1. Multistream approach of the transport equations, *J. Geophys. Res.*, *102*, 22,261–22,272.

Galand, M., J. Lilensten, W. Kofman, and D. Lummerzheim (1998), Proton transport model in the ionosphere: 2. Influence of magnetic mirroring and collisions on the angular redistribution in a proton beam, *Ann. Geophys.*, *16*, 1308–1321.

Galand, M., T. J. Fuller-Rowell, and M. V. Codrescu (2001), Response of the upper atmosphere to auroral protons, *J. Geophys. Res.*, *106*, 127–139.

Galand, M., D. Lummerzheim, A. W. Stephan, B. C. Bush, and S. Chakrabarti (2002), Electron and proton aurora observed spectroscopically in the far ultraviolet, *J. Geophys. Res.*, *107*(A7), 1129, doi:10.1029/2001JA000235.

Galand, M., J. Baumgardner, S. Chakrabarti, U. P. Løvhaug, B. Isham, J. Jussila, D. Lummerzheim, D. Evans, and F. Rich (2003), Proton aurora over EISCAT: Optical signature and associated ionospheric perturbations, in *Proceedings of the 30th Annual European Meeting on Atmospheric Studies by Optical Methods, August 13–17, 2003*, edited by F. Sigernes and D. A. Lorentzen, pp. 2–8, Univ. Courses on Svalbard Publ., Longyearbyen, Norway.

Haffner, L. M., R. J. Reynolds, and S. L. Tufte (1999), WHAM observations of $H\alpha$, [S II], and [N II] toward the Orion and Perseus arms: Probing the physical conditions of the warm ionized medium, *Astrophys. J.*, 523, 223–233.

Hardy, D. A., M. S. Gussenhoven, and R. Raistrick (1987), Statistical and functional representations of the pattern of auroral energy flux, number flux, and conductivity, *J. Geophys. Res.*, 92, 12,275–12,294.

Hardy, D. A., M. S. Gussenhoven, and D. Brautigam (1989), A statistical model of auroral ion precipitation, *J. Geophys. Res.*, 94, 370–392.

Hedin, A. E. (1991), Extension of the MSIS thermosphere model into the middle and lower atmosphere, *J. Geophys. Res.*, 96, 1159–1172.

Ishimoto, M., G. R. Romick, C.-I. Meng, and R. E. Huffman (1989), Doppler shift of auroral Lyman α observed from a satellite, *Geophys. Res. Lett.*, 16, 143–146.

Kerr, R. B., and J. H. Hecht (1996), Measurement of geocoronal Balmer alpha in the auroral zone, *J. Geophys. Res.*, 101, 189–194.

Kerr, R. B., et al. (2001a), Periodic variations of geocoronal Balmer-alpha brightness due to solar-driven exospheric abundance variations, *J. Geophys. Res.*, 106, 28,797–28,818.

Kerr, R. B., et al. (2001b), Secular variability of the geocoronal Balmer-alpha brightness: Magnetic activity and possible human influences, *J. Geophys. Res.*, 106, 28,819–28,830.

Kurucz, R. L., I. Furenlid, J. Brault, and L. Testerman (1984), Solar flux atlas from 296 to 1300 nm, in *National Observatory Atlas*, vol. 1, Nat. Sol. Observ., Sunspot, N. M.

Lanchester, B. S., M. Galand, S. C. Robertson, M. H. Rees, D. Lummerzheim, I. Furniss, L. M. Peticolas, H. U. Frey, J. Baumgardner, and M. Mendillo (2003), High resolution measurements and modeling of auroral hydrogen emission line profiles, *Ann. Geophys.*, 21, 1629–1643.

Lilensten, J., and M. Galand (1998), Proton-electron precipitation effects on the electron production and density above EISCAT (Tromsø) and ESR, *Ann. Geophys.*, 16, 1299–1307.

Lorentzen, D. A., F. Sigernes, and C. S. Deehr (1998), Modeling and observations of dayside auroral hydrogen emission Doppler profiles, *J. Geophys. Res.*, 103, 17,479–17,488.

Lummerzheim, D., and M. Galand (2001), The profile of the hydrogen H_β emission line in proton aurora, *J. Geophys. Res.*, 106, 23–31.

Lummerzheim, D., M. H. Rees, and G. J. Romick (1990), The application of spectroscopic studies of the aurora to thermospheric neutral composition, *Planet. Space Sci.*, 38, 67–78.

Meinel, A. B. (1951), Doppler-shifted auroral hydrogen emission, *Astrophys. J.*, 113, 50–54.

Mende, S. B., H. U. Frey, M. Lampton, J.-C. Gerard, B. Hubert, S. Fuselier, J. Spann, R. Gladstone, and J. L. Burch (2001), Global observations of proton and electron auroras in a substorm, *Geophys. Res. Lett.*, 28, 1139–1142.

Nossal, S., F. L. Roesler, J. Bishop, R. J. Reynolds, M. Haffner, S. Tufte, J. Percival, and E. J. Mierkiewicz (2001), Geocoronal H_α intensity measurements using the Wisconsin H_α Mapper Fabry-Perot facility, *J. Geophys. Res.*, 106, 5605–5616.

Pallamraju, D., J. Baumgardner, S. Chakrabarti, and T. R. Pedersen (2001), Simultaneous ground-based observations of an auroral arc in daytime/twilighttime OI 630.0 nm emission and by incoherent scatter radar, *J. Geophys. Res.*, 106, 5543–5549.

Pallamraju, D., J. Baumgardner, and S. Chakrabarti (2002), HIRISE: A ground-based high-resolution imaging spectrograph using echelle grating for measuring daytime airglow/auroral emissions, *J. Atmos. Sol. Terr. Phys.*, 64, 1581–1587.

Paresce, F., S. Chakrabarti, S. Bowyer, and R. Kimble (1983), The extreme ultraviolet spectrum of dayside and nightside aurorae: 800–1400 Å, *J. Geophys. Res.*, 88, 4905–4910.

Rees, M. H. (1982), On the interaction of auroral protons with the Earth's atmosphere, *Planet. Space Sci.*, 30, 463–472.

Rees, M. H. (1989), *Physics and Chemistry of the Upper Atmosphere*, Cambridge Atmos. Space Sci. Ser., Cambridge Univ. Press, New York.

Reynolds, R. J. (1997), Ionizing the galaxy, *Science*, 277, 1446–1447.

Samson, J. C., L. R. Lyons, P. T. Newell, F. Creutzberg, and B. Xu (1992), Proton aurora and substorm intensifications, *J. Geophys. Res.*, 19, 2167–2170.

Senior, C. (1991), Solar and particle contributions to auroral height-integrated conductivities from EISCAT data: A statistical study, *Ann. Geophys.*, 9, 449–460.

Sigernes, F., D. A. Lorentzen, C. S. Deehr, and K. Henriksen (1994a), Calculation of auroral Balmer volume emission height profiles in the upper atmosphere, *J. Atmos. Terr. Phys.*, 56, 503–508.

Sigernes, F., G. Fasel, C. S. Deehr, R. W. Smith, D. A. Lorentzen, L. T. Wetjen, and K. Henriksen (1994b), Proton aurora on the dayside, *Geomagn. Aeron.*, 34, 69–75.

Sigernes, F., G. Fasel, J. Minow, C. S. Deehr, R. W. Smith, D. A. Lorentzen, L. T. Wetjen, and K. Henriksen (1996), Calculations and ground-based observations of pulsed proton events in the dayside aurora, *J. Atmos. Terr. Phys.*, 58, 1281–1291.

Søraas, F., H. R. Lindalen, K. Mâseide, A. Egeland, T. A. Sten, and D. S. Evans (1974), Proton precipitation and the H_β emission in a postbreakup auroral glow, *J. Geophys. Res.*, 79, 1851–1859.

Srivastava, V., and V. Singh (1987), Model calculation of hydrogen Balmer emissions under various modes of proton precipitation, *Adv. Space Res.*, 70(8), 21–25.

Stamnes, K., and G. Witt (1985), The effect of light scattering and diffuse reflection on atmospheric spectral measurements, paper presented at the 13th Annual Meeting on Atmospheric Studies by Optical Methods, Oslo, Aug.

Strickland, D. J., R. E. Daniell Jr., J. R. Jasperse, and B. Basu (1993), Transport-theoretic model for the electron-proton-hydrogen atom aurora: 2. Model results, *J. Geophys. Res.*, 98, 21,533–21,548.

Strickland, D. J., J. Bishop, J. S. Evans, T. Majeed, R. J. Cox, D. Morrison, G. J. Romick, J. F. Carbary, L. J. Paxton, and C.-I. Meng (2001), Mid-course Space Experiment/Ultraviolet and Visible Imaging and Spectrographic Imaging limb observations of combined proton/hydrogen/electron aurora, *J. Geophys. Res.*, 106, 65–75.

Takahashi, Y., and H. Fukunishi (2001), The dynamics of the proton aurora in auroral breakup events, *J. Geophys. Res.*, 106, 45–63.

Vallance-Jones, A., F. Creutzberg, R. L. Gattinger, and F. R. Harris (1982), Auroral studies with a chain of meridian-scanning photometers: 1. Observations of proton and electron aurora in magnetospheric substorms, *J. Geophys. Res.*, 87, 4489–4503.

Van Zyl, B., and H. Neumann (1980), H_α and H_β emission cross sections for low-energy H and H^+ collisions with N_2 and O_2, *J. Geophys. Res.*, 85, 6006–6010.

Van Zyl, B., M. W. Gealy, and H. Neumann (1984), Prediction of photon yields for proton aurorae in an N_2 atmosphere, *J. Geophys. Res.*, 89, 1701–1710.

Vegard, L. (1948), Emission spectra of night sky and aurora, in *Reports of the Gassiot Committee*, p. 82, Phys. Soc. London, London.

Zwick, H. H., and G. G. Shepherd (1963), Some observations of hydrogen-line profiles in the aurora, *J. Atmos. Terr. Phys.*, 25, 604–607.

————————————

J. Baumgardner, S. Chakrabarti, M. Galand, and D. Pallamraju, Center for Space Physics, Boston University, 725 Commonwealth Avenue, Boston, MA 02215, USA. (jeff@spica.bu.edu; supc@bu.edu; mgaland@bu.edu; dpraju@bu.edu)

B. S. Lanchester and M. H. Rees, Department of Physics, University of Southampton, Highfield, Southampton SO17 1BJ, UK. (bsl@phys.soton.ac.uk; mhr@phys.soton.ac.uk)

U. P. Løvhaug, Department of Physics, The Auroral Observatory, University of Tromsø, Tromsø, N-9037, Norway. (unni.pia.lovhaug@phys.uit.no)

D. Lummerzheim, Geophysical Institute, University of Alaska, 903 Koyukuk Avenue North, Fairbanks, AK 99775-7320, USA. (lumm@gi.alaska.edu)